

Accelerated Article Preview

Double-side 2-dimensional/3-dimensional heterojunctions for inverted perovskite solar cells

Received: 22 May 2023

Accepted: 9 February 2024

Accelerated Article Preview

Cite this article as: Azmi, R. et al. Double-side 2-dimensional/3-dimensional heterojunctions for inverted perovskite solar cells. *Nature* <https://doi.org/10.1038/s41586-024-07189-3> (2024)

Randi Azmi, Drajad Satrio Utomo, Badri Vishal, Shynggys Zhumagali, Pia Dally, Andi Muhammad Risqi, Adi Prasetio, Esma Ugur, Fangfang Cao, Imil Fadli Imran, Ahmed Ali Said, Anil Reddy Pininti, Anand Selvin Subbiah, Erkan Aydin, Chuanxiao Xiao, Sang Il Seok & Stefaan De Wolf

This is a PDF file of a peer-reviewed paper that has been accepted for publication. Although unedited, the content has been subjected to preliminary formatting. Nature is providing this early version of the typeset paper as a service to our authors and readers. The text and figures will undergo copyediting and a proof review before the paper is published in its final form. Please note that during the production process errors may be discovered which could affect the content, and all legal disclaimers apply.

1 **Double-side 2-dimensional/3-dimensional heterojunctions for inverted**
2 **perovskite solar cells**

3 Randi Azmi,^{1*} Drajad Satrio Utomo,¹ Badri Vishal,¹ Shynggys Zhumagali,¹ Pia Dally,¹ Andi
4 Muhammad Risqi,² Adi Prasetyo,¹ Esma Ugur,¹ Fangfang Cao,³ Imil Fadli Imran,¹ Ahmed Ali
5 Said,¹ Anil Reddy Pininti,¹ Anand Selvin Subbiah,¹ Erkan Aydin,¹ Chuanxiao Xiao,^{3,4} Sang Il
6 Seok,² Stefaan De Wolf^{1*}

7
8 ¹King Abdullah University of Science and Technology (KAUST), KAUST Solar Center (KSC),
9 Physical Sciences and Engineering Division (PSE), Material Science and Engineering Program
10 (MSE), Thuwal, 23955-6900, Kingdom of Saudi Arabia

11 ²School of Energy and Chemical Engineering, Ulsan National Institute of Science and Technology
12 (UNIST), 50 UNIST-gil, Eonyang-eup, Ulju-gun, Ulsan, 44919 Republic of Korea

13 ³Ningbo Institute of Materials Technology and Engineering, Chinese Academy of Sciences,
14 Ningbo City, Zhejiang Province, 315201, China

15 ⁴Ningbo New Materials Testing and Evaluation Center CO., Ltd, Ningbo City, Zhejiang Province,
16 315201, China

17
18 *Corresponding authors: randi.azmi@kaust.edu.sa; stefaan.dewolf@kaust.edu.sa
19

20 **Abstract**

21 Defects at the top and bottom interfaces of three-dimensional (3D) perovskite photo-absorbers
22 diminish the performance and operational stability of perovskite solar cells (PSCs) due to charge
23 recombination, ion migration, and electric-field inhomogeneities.¹⁻⁵ Here, we demonstrate that
24 long alkyl-amine ligands can generate near-phase pure two-dimensional (2D) perovskites at the
25 top and bottom 3D perovskite interfaces and effectively resolves these issues. At the rear-contact
26 side, we find that the employed alkyl-amine ligand strengthens the interactions with the substrate
27 through acid-base reactions with the phosphonic acid group from the employed organic hole-
28 transporting self-assembled monolayer molecule, thus regulating the 2D perovskite formation.
29 With this, inverted PSCs with double-side 2D/3D heterojunctions achieved a power conversion
30 efficiency (PCE) of 25.6% (certified 25.0%), retaining 95% of their initial PCE after 1000 hours
31 of 1-sun illumination at 85 degrees Celsius in air.

32 **Main**

33 Engineering of perovskite interfaces is essential to enhance the performance and stability of
34 perovskite solar cells (PSCs). Two-/three-dimensional (2D/3D) perovskite heterojunctions have
35 shown particular promise towards this end.⁶⁻¹⁶ Usually, such heterojunctions are formed by post-
36 treating an as-deposited 3D perovskite film with a solution that contains 2D ligands to reconstruct
37 through cation exchange the 3D perovskite surface into a 2D perovskite.^{7-9,12,14} However, this
38 strategy is only applicable at the top surface of 3D perovskite films. Moreover, it usually results
39 in a 2D perovskite consisting of a mixture of multiple dimensionalities such as $n = 1, 2, 3, \text{etc.}$ with
40 random crystal orientations, where n refers to the number of subsequent corner-sharing octahedral
41 $[\text{PbI}_6]^{4-}$ inorganic slabs.^{8,12,14} Unfortunately, such mixed dimensionality may induce interfacial
42 energetic inhomogeneity and could impede charge transfer through band misalignment when such
43 a 2D/3D heterojunction is integrated into a charge-selective contact stack.^{7,8,12,14} In contrast, phase-
44 pure 2D perovskite passivation can substantially reduce the charge-trap density and ion migration,
45 leading to significantly improved device performance and stability.^{10,11} Hence, it is imperative to
46 narrow the distribution of the different n layers in 2D perovskites.^{10,11,16} Yet, achieving phase-pure
47 2D perovskite passivating contacts with a proper crystal orientation is experimentally
48 challenging.^{10,11,16}

49 Integrating 2D/3D heterojunctions at the buried bottom interface is desirable too, but has rarely
50 been reported to date.¹⁷⁻¹⁹ The primary difficulty here is to avoid the dissolution of the pre-
51 deposited 2D layer or the organic ammonium-based ligands during the subsequent 3D perovskite
52 deposition.¹⁷⁻¹⁹ Indeed, most organic ammonium ligands are readily dissolved into the highly polar
53 aprotic solvents typically used in 3D perovskite precursor inks such as dimethyl formamide (DMF)
54 and dimethyl sulfoxide (DMSO).^{11,20,21} Hence, one approach for minimizing the dissolution of 2D
55 ligands during perovskite solution casting is to strengthen their interaction with the substrate. This
56 allows for immobilizing 2D ligands prior to perovskite deposition, and forming a 2D perovskite
57 underneath the 3D perovskite film through cation exchange and intercalation of the 2D ligands
58 into the perovskite film, post deposition.

59 **2D/3D heterojunction at the bottom interface**

60 We developed inverted ($p-i-n$) PSCs with a hole-collecting contact (p -type) that is formed by
61 anchoring 2PACz, a self-assembled monolayer (SAM), onto the transparent bottom electrode,

62 consisting of indium-tin oxide (ITO). To resolve the challenge of 2D/3D heterojunction formation
63 at the bottom of the perovskite film, we mixed the HBzA ligand into the 2PACz SAM solution,
64 which was then coated onto the ITO bottom electrode. Here, we hypothesized that the amine head
65 of the HBzA molecule would react with the phosphonic acid ($-\text{PO}(\text{OH})_2$) group of the 2PACz,
66 forming an ionic bond, resilient against subsequent processing. This acid-base reaction is favorable
67 with the lower values of the negative log of the acid dissociation constant for the first proton ($\text{p}K_{\text{a1}}$)
68 of the phosphonic acid (~ 2.5) and the negative log of the base dissociation constant ($\text{p}K_{\text{b}}$) of alkyl-
69 amines (~ 3.6).^{22,23} We note that only the first proton transfer is favorable between 2PACz and
70 HBzA, owing to a higher $\text{p}K_{\text{a2}}$ value of the second proton (~ 8.5).²² We experimentally verified that
71 the abovementioned reaction takes place in the mixture of 2PACz and HBzA, as discussed in
72 **Extended Data Fig. 1a–b**. Moreover, the $-\text{OH}$ group from HBzA can form hydrogen bonds with
73 $-\text{PO}(\text{OH})_2$ and ITO, thus strengthening the attachment further.²⁴ The detailed explanation of all
74 these mechanisms is in **Fig. 1a**.

75 We then investigated the chemical properties of HBzA and 2PACz molecules on ITO using X-ray
76 photoelectron spectroscopy (XPS). The high-resolution spectrum of the carbon region (C1s) of
77 HBzA shows the presence of C=C, C–N, and C–OH bonds that correspond to the aromatic ring,
78 amine head, and the phenol group of HBzA, respectively (**Extended Data Fig. 1c**). Further, C1s
79 spectra of 2PACz feature the signature of C–P bonds, corresponding to its $-\text{PO}(\text{OH})_2$ group. These
80 identical features of 2PACz and HBzA were also found after their mixture was coated on ITO,
81 indicating the presence of both molecules. To strengthen our hypothesis, we also did a washing
82 test on the ITO/HBzA and ITO/(HBzA+2PACz) samples with a highly polar aprotic DMF/DMSO
83 solvent mixture that can easily solvate HBzA molecules by forming strong hydrogen bonding. We
84 observed that if only HBzA layers are anchored on ITO, they could be easily washed away.
85 However, the presence of 2PACz significantly enhances the attachment of HBzA onto the ITO
86 surface, as indicated by a qualitative analysis of the marginal reduction of the atomic ratio of
87 nitrogen to indium (N/In) after washing (**Supplementary Table 1**). This supports our hypothesis
88 that HBzA and 2PACz form an ionic bonding through proton transfer from phosphonic acid to the
89 amine group. This bonding facilitates their adherence to the substrate during perovskite processing
90 and assists in the formation of a 2D perovskite layer beneath the 3D perovskite layer.

91 After successfully attaching HBzA ligands on the ITO/2PACz surface, we deposited the 3D
92 perovskite ink via spin-coating. The HBzA ligands are liberated after 3D perovskite deposition,
93 initiating the 2D perovskite formation at the bottom interface through cation exchanges between
94 HBzA⁺ and formamidinium (FA⁺) or caesium (Cs⁺) of the 3D perovskite ink. This cation exchange
95 process is completed during the thermal annealing of perovskite films at 120 °C for 30 min to
96 crystallize the 2D/3D perovskite film. To prove this mechanism, we completely removed the
97 resulting perovskite layers from the ITO/2PACz/2D-HBzA/3D-perovskite structure by washing
98 the samples with a DMF/DMSO solution and measured the work function (WF) of the resulting
99 structure using kelvin-probe-force microscopy (KPFM). We noted that the WF of bare
100 ITO/(2PACz+HBzA) sample remained similar before and after washing with DMF/DMSO (5.08
101 eV, **Extended Data Fig. 2a–c**). However, after the perovskite film deposition and subsequent
102 removal of the HBzA ligands, the WF of ITO/(2PACz+HBzA) is shifted to 5.42 eV, closer to the
103 WF of pristine ITO/2PACz (5.40 eV) with identical conditions (**Extended Data Fig. 2d–e**). This
104 indicates that DMF/DMSO alone was not sufficient to remove HBzA molecules. Rather, the
105 removal was facilitated by the 3D perovskite deposition, corroborating our hypothesis that 2D
106 ligands are released only after perovskite film formation.

107 The cross-sectional high-resolution scanning transmission electron microscopy (HR-STEM)
108 images in **Fig. 1b** reveal the formation of a discontinuous 2D perovskite layer at the bottom
109 interface between ITO/2PACz and 3D perovskite layers. The discontinuity of 2D perovskite layers
110 might be related to their complex formation mechanism, such as random distribution of HBzA
111 molecules and their release during cation exchange. We further analyzed the 2D/3D perovskite
112 heterojunction at the bottom-side interface by photoluminescence (PL) spectroscopy and observed
113 distinct PL emission peaks for 2D perovskite at ~570 nm and ~520 nm corresponding to $n = 2$ and
114 $n = 1$, respectively (**Fig. 1c**).¹² The significantly high PL emission intensity of $n = 2$ indicates the
115 dominant formation of near-phase pure 2D perovskite layers. In addition, we performed PL
116 mapping at ~570 nm with different concentrations of HBzA ligand and observed discontinuities
117 for 2D perovskite crystal PL emission at the bottom interface (**Supplementary Fig. 1**), in
118 accordance with HR-STEM results.

119 We further analyzed the structural properties and chemical composition of 2D perovskite at the
120 bottom-side interface by gently separating the bottom-side 2D/3D perovskite film from the
121 ITO/hole-selective surface using the lift-off technique following previous report.²⁵ This approach

122 preserves the chemical and structural integrity of the film (see the schematics of the process in
123 **Supplementary Fig. 2a**). We then characterized the bottom-side perovskite film by scanning
124 electron microscopy (SEM) and XPS measurements. SEM top-view images of the lift-off samples
125 show no distinctive morphological damage to the control and 2D/3D heterojunction samples
126 (**Supplementary Fig. 2b**). However, we note that the crystal grain-sizes of perovskite of 2D/3D
127 samples are larger ($1.64 \pm 0.31 \mu\text{m}$) compared to control perovskite ($0.93 \pm 0.20 \mu\text{m}$), indicating
128 that 2D perovskite formation at the bottom interface also regulates the crystallization of the
129 overlying 3D perovskite film.²⁶ Further, the XPS analysis of 2D/3D samples revealed the presence
130 of C–O and C–N bonds at 286.5 and 285.6 eV, associated with HBzA ligands (**Supplementary**
131 **Fig. 2c**).

132

133 **3D/2D heterojunction at the top interface**

134 For the 3D/2D heterojunction at the top interface, we developed a simple two-step hybrid method
135 to form phase-pure 2D perovskite layers. This process initially involves depositing the PbI_2 layer
136 with controlled thickness via vacuum evaporation on top of the as-prepared 3D perovskite film
137 (see **Fig. 2a**, step (i)). This is then followed by dropping the HBzA salt or mixture of HBzA
138 salt+FAI solutions on top of perovskite/ PbI_2 film in step (ii). Finally, the samples are thermally
139 annealed to form a 2D perovskite layer with controllable dimensionality and phase purity in step
140 (iii).

141 **Fig. 2b** shows the normalized PL spectra of 3D/2D perovskite films for two conditions. First, when
142 coating the HBzA salt cation-only solution, the 3D/2D perovskite sample shows a single emission
143 peak at a low wavelength $\sim 520 \text{ nm}$ (corresponding to $n = 1$).^{8,12,27} Second, the sample based on the
144 mixture of HBzA salt+FAI also shows a single emission peak but at a higher wavelength (~ 570
145 nm), which corresponds to $n = 2$.^{8,12} These results confirm the success of our method to control
146 the phase-purity and dimensionality of 2D perovskites, which to date remained a challenge.^{7,8,12,14}
147 In contrast, the conventional method by direct coating of HBzA salt solution on top of 3D
148 perovskite followed only steps (ii) and (iii) (with the absence of PbI_2 deposition) forms a mixture
149 of multiple dimensionalities of 2D-perovskite ($n = 1, 2, \text{ and } 3$; **Supplementary Fig. 3**), consistent
150 with previous works.^{8,12} We note that a higher dimensionality of the 2D perovskite ($n > 1$)

151 passivation layer is critical, owing to a higher conductivity by having less bulky-organic cations
152 interfaces.^{8,11,12}

153 Next, we identified the crystal orientation and dimensionality of the 2D perovskite layers through
154 grazing-incidence wide-angle X-ray scattering (GIWAXS) measurements. **Fig. 2c** shows the
155 diffraction map of GIWAXS of the 3D/2D sample with strong diffraction peaks at lower q_z (0.31
156 \AA^{-1} and 0.64\AA^{-1}) representing the (002) and (004) planes of 2D perovskite ($n = 2$), respectively,
157 with a layer spacing d of $\sim 20.3 \text{\AA}$ and $\sim 9.8 \text{\AA}$.^{13,14,28,29} Interestingly, strong and more discrete
158 Bragg spots at a higher q_z ($\sim 1.5 \text{\AA}^{-1}$ and $\sim 1.7 \text{\AA}^{-1}$) were observed in the 3D/2D sample. This
159 indicates the improved orientation of the 2D perovskite corresponding to the (282), (121), and
160 (082) planes, formed with perpendicular orientation to the 3D perovskite underneath, as
161 highlighted with oval dot lines.^{30,31} In contrast, we do not observe the diffraction peaks at lower q_z
162 and discrete Bragg spots in control perovskite samples (**Supplementary Fig. 4a–b**). This result is
163 also consistent with the X-ray diffraction pattern of phase-pure 2D perovskite thin film, as shown
164 in **Supplementary Fig. 4c–d**. Further, we visualize the 2D perovskite formation and orientation
165 at the top-contact using cross-sectional HR-STEM in **Fig. 2d**, with a predominantly perpendicular
166 orientation. In addition, a thin layer of 2D perovskite does not change the morphology of 3D
167 perovskite underneath (**Supplementary Fig. 5**), suggesting the robustness of our hybrid method
168 to form perovskite heterostructures.

169

170 **Device performance and characterizations**

171 After successfully completing the near-phase pure 2D perovskite passivation layers at the bottom
172 and top 3D perovskite interfaces, we adopted them to PSCs with a structure of ITO/2PACz/2D-
173 perovskite/3D-perovskite/2D-perovskite/C₆₀/BCP/Ag (**Fig. 3a**). We first tested various alkyl-
174 amine-based 2D ligands with different concentrations with respect to the ratio between 2PACz
175 SAM and 2D ligands at the bottom-side 2D/3D passivation, as shown from the statistical analysis
176 of devices performance in **Extended Data Fig. 3a–b**. The device results revealed that the optimum
177 concentration of the 2D ligand at the bottom contact is around a 1:1 molar ratio with 2PACz SAM.
178 The higher concentration of 2D ligand at the bottom interface leads to a thicker 2D perovskite
179 layer, lowering the FF of devices. This is likely due to the nature of higher resistance of long-alkyl
180 ligands in parallel orientation to the 3D perovskite layer, which can inhibit charge transport.³²

181 Interestingly, among the five alkyl-amine ligands tested, the HBzA ligand gives the highest
182 performance, potentially due to the addition of an –OH group that could form a hydrogen bond
183 with –PO(OH)₂ and ITO or coordinate with 3D perovskite at the 2D/3D interface.^{33,34} The longer
184 2D ligand (*i.e.*, hexylmethylamine) results in the lower performance, potentially due to a higher
185 charge transfer resistivity induced by long-alkyl ligand. This suggests the critical roles of
186 additional functional groups and the design of the proper size of 2D ligands for bottom
187 passivation.^{8,16}

188 Next, we fabricated the top-side 3D/2D heterojunction using the abovementioned hybrid method.
189 Here, we deposited PbI₂ with different thicknesses (7, 15, and 25 nm) and found the thickness of
190 2D perovskite will depend on the initial thickness of the inorganic PbI₂ layer. Based on the device
191 results, it is found that 15 nm-thick PbI₂ film results in 35 nm-thick 2D perovskite layer, which is
192 optimal for top-side passivation (**Extended Data Fig. 3c**). In contrast, a 25 nm PbI₂ film forms
193 thicker 2D perovskite (around 55 nm, see cross-sectional SEM image in **Supplementary Fig. 6**),
194 which slows down the charge transfer/extraction rate at the perovskite/C₆₀ interface. It is consistent
195 with the decreased FF values from these devices, as indicated by the transient PL measurement
196 and differential lifetime analysis in **Supplementary Fig. 7**.

197 We then investigated the relation between the 2D perovskite orientation and charge transfer and
198 extraction rates. For this, we compared the charge transfer and extraction rates between the 3D
199 perovskite and C₆₀ when a 35 nm-thick 2D perovskite layer prepared by hybrid and solution post-
200 treatment methods is inserted between them. It should be noted that the 2D perovskite layer
201 prepared with solution post-treatment method has a parallel orientation to the 3D perovskite
202 surface, which significantly hinders charge transport, and limits the thickness of the 2D
203 layer.^{8,11,12,16,35}

204 The charge transfer and extraction at the interfaces also depend on the energetic alignment between
205 3D perovskite and charge-selective contacts (**Extended Data Fig. 4a**). With the two-step hybrid
206 method, the secondary electron-cut-off of 2D perovskite shifted to lower binding energy
207 (**Extended Data Fig. 4b**). As a result, the conduction band minimum (CBM) of top-side phase-
208 pure 2D perovskite ($n = 2$) prepared by the hybrid method was deeper compared to the previously
209 reported mix-phase of 2D perovskite top-contact passivation using the conventional solution post-
210 treatment method, which resulted in dramatically minimizing the electron barrier.^{8,12,16} Further,

211 the slightly deeper valence band maximum (VBM) of the bottom-side 2D perovskite compared to
212 the control 3D perovskite is favourable for hole transfer at the ITO/2PACz contact interface
213 **(Extended Data Fig. 4c–d)**.

214 We then adopted double-side 2D/3D heterojunction passivation to our inverted PSCs and
215 demonstrated a maximum PCE of 25.63% ($V_{OC} = 1.19$ V, $J_{SC} = 24.94$ mA cm⁻², and FF = 85.9%,
216 see **Fig. 3b**) under reverse scan and stabilized PCE of 25.1% using triple-cation
217 Cs_{0.025}MA_{0.075}FA_{0.90}PbI₃ perovskite with a bandgap of 1.53 eV (**Supplementary Fig. 8**). This
218 result represents an absolute ~2.3% PCE enhancement compared to control devices (PCE around
219 23.3%) and >1% to only top- or only bottom-side 2D/3D heterojunction with PCE around 24%.^{8,10-}
220 ¹² **Fig. 3c** shows the statistical analysis results of the PCE, V_{OC} , and FF values from 25 devices for
221 each condition. We demonstrated the universality of our approach by testing various hole-
222 transporting SAM molecules (*i.e.*, 2PACz, MeO-2PACz, and 4PADCB) and other perovskite
223 compositions of Cs_{0.05}FA_{0.95}PbI₃ (~1.54 eV) with PCEs reaching up to 25% for each condition, as
224 shown from the statistical analysis of devices in **Supplementary Figs. 9** and **Extended Data Fig.**
225 **5**, respectively. We also confirmed the high process robustness of our approaches by showing less
226 than 1% PCE deviation from person-to-person, performed by three different researchers
227 (**Supplementary Fig. 10**). The performance of the double-side 2D/3D heterojunction passivated
228 solar cells were verified by an independently accredited testing center by presenting a PCE of
229 25.00% ($V_{OC} = 1.17$ V, $J_{SC} = 25.00$ mA cm⁻², and FF = 85.7% under reverse current-voltage scan,
230 **Supplementary Fig. 11**). This result represents one of the highest certified efficiencies in inverted
231 PSCs in current literature (**Supplementary Table 2**).

232 Notably, the $V_{OC} \times FF$ value of our double-side 2D/3D heterojunctions-based device was around
233 91% with respect to the Shockley–Queisser limit, one of the highest values among PSCs with only
234 top-side or bulk passivation (**Supplementary Fig. 12**). The high V_{OC} and FF values of the devices
235 can be associated with the low charge recombination and traps at the top and bottom interfaces.^{15,36}
236 First, we measured the PL quantum yield (PLQY) to demonstrate the quality of perovskite film
237 before and after 2D perovskite passivation. The substantially improved PLQY of the double-side
238 2D/3D passivation ($6.67\% \pm 0.58\%$) confirms the high quality of 2D/3D/2D perovskite film
239 compared to control perovskite sample ($1.84\% \pm 0.63\%$) and one-side 2D/3D passivation sample
240 only (**Extended Data Fig. 6a**). Even after adding the C₆₀ layer, the maintained a high PLQY value
241 of double-side 2D/3D perovskite ($5.78\% \pm 0.33\%$) versus the control sample (significantly

242 dropped around $0.19\% \pm 0.06\%$), demonstrating the improved optoelectronic quality of perovskite
243 layer with the full stack of devices. This suggests that the 2D perovskite passivation layer can
244 efficiently suppress the charge recombination at these interfaces. These results are also consistent
245 with the longer Shockley-Read-Hall lifetime of double-side 2D/3D heterojunctions ($2.69 \mu\text{s}$),
246 around three and two times longer versus control ($0.97 \mu\text{s}$), and only one-side passivation ($1.34 \mu\text{s}$
247 and $1.73 \mu\text{s}$ for the bottom- and top-side only passivation, respectively), as shown in **Extended**
248 **Data Fig. 6b**.

249 We also determined the trap states for control and double-side 2D/3D passivation of perovskite
250 films using space-charge-limited-current (SCLC) and thermal admittance spectroscopy (TAS)
251 analyses.^{12,37} For the SCLC, we fabricated the electron-only (ITO/SnO₂/perovskite/C₆₀/BCP/Ag)
252 and hole-only (ITO/SAM/perovskite/PTAA/MoO_x/Ag) devices to estimate the trap densities of
253 perovskite films. The trap-filled limited voltage (V_{TFL}) of double-side 2D/3D passivation samples
254 was more than 2-fold lower than control samples for both electron- and hole-only devices
255 (**Extended Data Fig. 6c–d**), indicating reduced trap density states (N_t) for both electron- and hole-
256 only devices (see **Supplementary Note 1**). This result suggests reduced negative and positive
257 defects at both interfaces with 2D perovskite passivation. It should be noted that the SCLC analysis
258 has limitations in extracting the exact value of N_t due to the presence of mobile ions in perovskite
259 materials.³⁸ Therefore, we also performed TAS analysis to quantify the N_t of perovskite films
260 relative to their energetic defect levels.^{12,37} Overall, the N_t of double-side 2D/3D perovskite
261 passivation-based devices has lower N_t values in all energetic defect levels, suggesting sufficient
262 passivation of shallow and deep levels of defect in perovskite film by 2D perovskite passivation
263 (**Extended Data Fig. 6e**).

264 Further, the defects at the interfaces of perovskite films can affect to charge accumulation and
265 electric-field inhomogeneity of perovskite devices.^{1,3-5,37} We then analyzed the capacitance–
266 voltage under various light illumination intensities to evaluate charge dynamics at the interfaces
267 (**Supplementary Fig. 13**). The shift in peak-potential (V_{peak}) under reverse bias with respect to the
268 illumination intensity reflected the degree of interfacial charge accumulation, which was due to
269 interfacial charge trapping.³⁷ Marginal shifting of the V_{peak} in the double-side 2D/3D device
270 indicated a reduced charge accumulation (less charge trapping) compared to the control device
271 (larger V_{peak} shifting), consistent with the above results. Interestingly, from the cross-sectional
272 KPFM mapping (**Fig. 3d and 3e**), stronger electric-field differences after 2D perovskite insertion

273 at the perovskite/C₆₀ contact further prove a lower interfacial defect density.³⁹ We note that the
274 electric-field extended further into the perovskite film, more effectively repelling holes and thus
275 suppressing recombination at the perovskite/C₆₀ interface.⁴⁰ We note that a similar electric-field
276 strength difference is observed at the 2PACz/perovskite contact for both control and double-side
277 passivation devices, presumably due to the higher dipole of 2PACz SAMs.³⁹ However, a uniform
278 electric-field is observed after 2D perovskite insertion at 2PACz/perovskite contact, as indicated
279 by a single peak. Consequently, this aids in charge transfer/extraction and leads to enhance *V*_{oc}
280 and FF values of devices.

281 **Stability and ion migration analyses**

282 We evaluated the long-term stability of encapsulated PSCs under light and thermal stresses. First,
283 **Fig. 3f** shows the stability under the open-circuit condition at 1-sun and 85 °C of the devices in air
284 (with a relative humidity of ~50%). The double-side 2D/3D heterojunction devices delivered a
285 relative PCE loss of only 5% after more than 1000 h. In contrast, the bottom- and top-side
286 passivation-based devices retain around 75% and 86% from their initial PCEs, respectively, versus
287 the control devices (without any 2D/3D heterojunction) retain around only 35% under identical
288 conditions. This result indicates the importance of passivating perovskite film's top and bottom
289 interfaces to improve their stability. Further, we measured the operational stability of double-side
290 2D/3D heterojunctions device under maximum-power-point tracking (MPPT). Around 90% of
291 their original PCE was retained after the PCE tracking for over 1000 h under 1-sun at 40 °C (**Fig.**
292 **3g**).

293 The degradation of perovskites under illumination and thermal stress can be related to defect-
294 induced ion migrations.^{1,25,37,41} First, the defects related to iodine generation and migration were
295 investigated under 1-sun illumination at 85 °C. It has been reported that the significant release of
296 iodine compound from perovskite film during light soaking at elevated temperature is mainly due
297 to interstitial iodide or PbI₂ defects.^{25,41} Passivating those defects by double-side 2D/3D
298 passivation suppresses the iodine generation/migration in perovskite films. This is proved by the
299 lowering intensity of UV-vis absorption spectrum of iodine at the maximum peak of wavelength
300 around 500 nm after immersing the perovskite films into toluene solution to light and heat
301 (**Extended Data Fig. 7a–b**).^{25,41}

303 Finally, the activation energy for ion migration was obtained to reveal the ion-induced migration
304 character in 2D/3D and control 3D perovskite films using temperature-dependent conductivity
305 measurement.³⁷ The activation energy value of the control 3D perovskite was fitted to be 0.27 eV,
306 in agreement with a previously reported value. In contrast, the activation energy value for the
307 double-side 2D/3D heterojunctions film is increased to 0.47 eV (**Extended Data Fig. 7c**). This
308 result indicates that the double-side 2D/3D heterojunctions have a significantly boosted energy
309 barrier for ion migration, which might also improve the perovskite crystal stability.

310

311 References

- 312 1 Ni, Z. *et al.* Evolution of defects during the degradation of metal halide perovskite solar
313 cells under reverse bias and illumination. *Nature Energy* **7**, 65–73, doi:10.1038/s41560-
314 021-00949-9 (2022).
- 315 2 Ni, Z. *et al.* Resolving spatial and energetic distributions of trap states in metal halide
316 perovskite solar cells. *Science* **367**, 1352–1358, doi:10.1126/science.aba0893 (2020).
- 317 3 Chen, H. *et al.* Regulating surface potential maximizes voltage in all-perovskite tandems.
318 *Nature* **613**, 676–681, doi:10.1038/s41586-022-05541-z (2023).
- 319 4 Jiang, Q. *et al.* Surface reaction for efficient and stable inverted perovskite solar cells.
320 *Nature* **611**, 278–283, doi:10.1038/s41586-022-05268-x (2022).
- 321 5 Tan, S. *et al.* Stability-limiting heterointerfaces of perovskite photovoltaics. *Nature* **605**,
322 268–273, doi:10.1038/s41586-022-04604-5 (2022).
- 323 6 Jung, E. H. *et al.* Efficient, stable and scalable perovskite solar cells using poly(3-
324 hexylthiophene). *Nature* **567**, 511–515, doi:10.1038/s41586-019-1036-3 (2019).
- 325 7 Yang, G. *et al.* Stable and low-photovoltage-loss perovskite solar cells by multifunctional
326 passivation. *Nature Photonics* **15**, 681–689, doi:10.1038/s41566-021-00829-4 (2021).
- 327 8 Chen, H. *et al.* Quantum-size-tuned heterostructures enable efficient and stable inverted
328 perovskite solar cells. *Nature Photonics* **16**, 352–358, doi:10.1038/s41566-022-00985-1
329 (2022).
- 330 9 Luo, L. *et al.* Stabilization of 3D/2D perovskite heterostructures via inhibition of ion
331 diffusion by cross-linked polymers for solar cells with improved performance. *Nature*
332 *Energy* **8**, 294–303, doi:10.1038/s41560-023-01205-y (2023).
- 333 10 Jang, Y.-W. *et al.* Intact 2D/3D halide junction perovskite solar cells via solid-phase in-
334 plane growth. *Nature Energy* **6**, 63–71, doi:10.1038/s41560-020-00749-7 (2021).
- 335 11 Sidhik, S. *et al.* Deterministic fabrication of 3D/2D perovskite bilayer stacks for durable
336 and efficient solar cells. *Science* **377**, 1425–1430, doi:10.1126/science.abq7652 (2022).
- 337 12 Azmi, R. *et al.* Damp heat-stable perovskite solar cells with tailored-dimensionality 2D/3D
338 heterojunctions. *Science* **376**, 73–77, doi:10.1126/science.abm5784 (2022).

- 339 13 Niu, T. *et al.* Spacer engineering of diammonium-based 2D perovskites toward efficient
340 and stable 2D/3D heterostructure perovskite solar cells. *Advanced Energy Materials* **12**,
341 2102973, <https://doi.org/10.1002/aenm.202102973> (2022).
- 342 14 Proppe, A. H. *et al.* Multication perovskite 2D/3D interfaces form via progressive
343 dimensional reduction. *Nature Communications* **12**, 3472, doi:10.1038/s41467-021-
344 23616-9 (2021).
- 345 15 Azmi, R. *et al.* Moisture-resilient perovskite solar cells for enhanced stability. *Advanced*
346 *Materials* 2211317, <https://doi.org/10.1002/adma.202211317> (2023).
- 347 16 Gu, H. *et al.* Phase-pure two-dimensional layered perovskite thin films. *Nature Reviews*
348 *Materials* **8**, 533–551, doi:10.1038/s41578-023-00560-2 (2023).
- 349 17 Yang, X. *et al.* Buried interfaces in halide perovskite photovoltaics. *Advanced Materials*
350 **33**, 2006435, <https://doi.org/10.1002/adma.202006435> (2021).
- 351 18 Mahmud, M. A. *et al.* Cation-diffusion-based simultaneous bulk and surface passivations
352 for high bandgap inverted perovskite solar cell producing record fill factor and efficiency.
353 *Advanced Energy Materials* **12**, 2201672, <https://doi.org/10.1002/aenm.202201672>
354 (2022).
- 355 19 Mahmud, M. A. *et al.* Double-sided surface passivation of 3D perovskite film for high-
356 efficiency mixed-dimensional perovskite solar cells. *Advanced Functional Materials* **30**,
357 1907962, <https://doi.org/10.1002/adfm.201907962> (2020).
- 358 20 Wu, S. *et al.* Modulation of defects and interfaces through alkylammonium interlayer for
359 efficient inverted perovskite solar cells. *Joule* **4**, 1248–1262,
360 <https://doi.org/10.1016/j.joule.2020.04.001> (2020).
- 361 21 Degani, M. *et al.* 23.7% efficient inverted perovskite solar cells by dual interfacial
362 modification. *Science Advances* **7**, eabj7930, doi:10.1126/sciadv.abj7930 (2021).
- 363 22 Kyuji, O. Prediction of pKa values of alkylphosphonic acids. *Bulletin of the Chemical*
364 *Society of Japan* **65**, 2543–2545, doi:10.1246/bcsj.65.2543 (1992).
- 365 23 Dorner, R. W., Deifallah, M., Coombes, D. S., Catlow, C. R. A. & Corà, F. Synthesis and
366 structure determination of a novel layered aluminophosphate material templated with 1-
367 phenylethylamine: [AlPO₄(OH)](NH₃C₂H₄C₆H₅). *Chemistry of Materials* **19**, 2261–2268,
368 doi:10.1021/cm070106u (2007).
- 369 24 Szatyłowicz, H. Structural aspects of the intermolecular hydrogen bond strength: H-bonded
370 complexes of aniline, phenol and pyridine derivatives. *Journal of Physical Organic*
371 *Chemistry* **21**, 897–914, <https://doi.org/10.1002/poc.1394> (2008).
- 372 25 Chen, S. *et al.* Stabilizing perovskite-substrate interfaces for high-performance perovskite
373 modules. *Science* **373**, 902–907, doi:10.1126/science.abi6323 (2021).
- 374 26 Li, H. *et al.* 2D/3D heterojunction engineering at the buried interface towards high-
375 performance inverted methylammonium-free perovskite solar cells. *Nature Energy* **8**, 946–
376 955, doi:10.1038/s41560-023-01295-8 (2023).

- 377 27 Stolterfoht, M. *et al.* The impact of energy alignment and interfacial recombination on the
378 internal and external open-circuit voltage of perovskite solar cells. *Energy &*
379 *Environmental Science* **12**, 2778–2788, doi:10.1039/C9EE02020A (2019).
- 380 28 Alanazi, A. Q. *et al.* Benzylammonium-mediated formamidinium lead iodide perovskite
381 phase stabilization for photovoltaics. *Advanced Functional Materials* **31**, 2101163,
382 <https://doi.org/10.1002/adfm.202101163> (2021).
- 383 29 Cao, D. H., Stoumpos, C. C., Farha, O. K., Hupp, J. T. & Kanatzidis, M. G. 2D homologous
384 perovskites as light-absorbing materials for solar cell applications. *Journal of the American*
385 *Chemical Society* **137**, 7843–7850, doi:10.1021/jacs.5b03796 (2015).
- 386 30 Quintero-Bermudez, R. *et al.* Compositional and orientational control in metal halide
387 perovskites of reduced dimensionality. *Nature Materials* **17**, 900–907,
388 doi:10.1038/s41563-018-0154-x (2018).
- 389 31 Tsai, H. *et al.* High-efficiency two-dimensional Ruddlesden–Popper perovskite solar cells.
390 *Nature* **536**, 312–316, doi:10.1038/nature18306 (2016).
- 391 32 Chen, Y. *et al.* Tailoring organic cation of 2D air-stable organometal halide perovskites for
392 highly efficient planar solar cells. *Advanced Energy Materials* **7**, 1700162,
393 <https://doi.org/10.1002/aenm.201700162> (2017).
- 394 33 Wang, Y. *et al.* Stabilizing heterostructures of soft perovskite semiconductors. *Science* **365**,
395 687–691, doi:10.1126/science.aax8018 (2019).
- 396 34 Cohen, B.-E. *et al.* Hydroxyl functional groups in two-dimensional dion–jacobson
397 perovskite solar cells. *ACS Energy Letters* **7**, 217–225, doi:10.1021/acsenerylett.1c01990
398 (2022).
- 399 35 Zhao, W. *et al.* Orientation engineering via 2D seeding for stable 24.83% efficiency
400 perovskite solar cells. *Advanced Energy Materials* **13**, 2204260,
401 <https://doi.org/10.1002/aenm.202204260> (2023).
- 402 36 Zhang, Z. *et al.* Rationalization of passivation strategies toward high-performance
403 perovskite solar cells. *Chemical Society Reviews* **52**, 163–195, doi:10.1039/D2CS00217E
404 (2023).
- 405 37 Azmi, R. *et al.* Shallow and deep trap state passivation for low-temperature processed
406 perovskite solar cells. *ACS Energy Letters* **5**, 1396–1403,
407 doi:10.1021/acsenerylett.0c00596 (2020).
- 408 38 Le Corre, V. M. *et al.* Revealing charge carrier mobility and defect densities in metal halide
409 perovskites via space-charge-limited current measurements. *ACS Energy Letters* **6**, 1087–
410 1094, doi:10.1021/acsenerylett.0c02599 (2021).
- 411 39 Zheng, X. *et al.* Co-deposition of hole-selective contact and absorber for improving the
412 processability of perovskite solar cells. *Nature Energy* **8**, 462–472, doi:10.1038/s41560-
413 023-01227-6 (2023).
- 414 40 Hou, Y. *et al.* Efficient tandem solar cells with solution-processed perovskite on textured
415 crystalline silicon. *Science* **367**, 1135–1140, doi:10.1126/science.aaz3691 (2020).

416 41 Lin, Y.-H. *et al.* A piperidinium salt stabilizes efficient metal-halide perovskite solar cells.
417 *Science* **369**, 96–102, doi:10.1126/science.aba1628 (2020).

418

419 Figure legends

420 **Fig. 1: 2D/3D heterojunction at hole-selective bottom interface** | **a**, Scheme showing the
421 mechanism of 3D-perovskite formation on ITO/2PACz+HBzA and cation exchange at the bottom
422 interface (left-hand-side); 2D/3D heterojunction on ITO/2PACz bottom-contact (right-hand-side).
423 **b**, Cross-sectional High-angle annular dark-field (HAADF)-STEM image of near bottom HTL
424 contact with zoom-in of the area showing the parallel 2D perovskite layers. Fast Fourier transform
425 (FFT) shows 2D inter-planar spots (002) and (004) are matched with the dominant phase of $n = 2$.
426 **c**, Normalized PL spectra of bottom-side 2D/3D from low to high wavelengths with different
427 excitation directions from the glass-side and top perovskite surface film using 405 nm excitation.

428 **Fig. 2: 3D/2D heterojunction at electron-selective top interface** | **a**, Sketch explaining two-step
429 hybrid process to form 3D/2D heterojunction perovskites. **b**, Normalized PL spectra of each film
430 with light direction from the top perovskite surface film. **c**, GIWAXS maps of top-side 3D/2D
431 heterojunction at a low incidence angle (0.2°). **d**, Cross-sectional HAADF-STEM image of near
432 top C₆₀-contact with zoom-in of the area showing the perpendicular orientation of 2D-perovskite.

433 **Fig. 3: Device performance and stability analyses** | **a**, Sketch of the fabricated single-junction
434 PSC. **b**, Representative $J-V$ curve for control, bottom, top, and double-side 2D/3D heterojunctions
435 PSC. **c**, Statistics parameters of PCE, V_{OC} , and FF (from top to bottom) values of PSCs. The box
436 and whisker plots indicate the statistical distribution: the center line represents the average value;
437 the bottom and top of the box represent the 25% to 75% percentiles; the small square represents
438 the mean; the whiskers represent outliers. **d**, **e**, Electric field distribution through both interfaces
439 from C₆₀-ETL to glass/ITO side acquired via KPFM cross-section scans. We mapped the photo-
440 voltage of the cells illuminated by an LED light. Note that we break the hole- and electron-selective
441 peaks for better visualization. **f**, Stability of encapsulated control bottom, top, and double-side
442 2D/3D passivation-based devices under 1-sun illumination at 85 °C and open-circuit conditions.
443 Five cells were used to construct the statistic, with the average represented by the symbol and the
444 standard deviation by the error bar. **g**, MPPT of an encapsulated double-side 2D/3D passivation-
445 based device under 1-sun illumination at 40 °C.

446

447 Methods

448 Materials

449 Dimethylformamide (DMF, 99.8%, anhydrous), dimethylsulfoxide (DMSO, 99.9%, anhydrous),
450 potassium chloride (KCl, 99.9%), 4-Hydroxybenzylamine (HBzA, C₇H₉NO), benzylamine,
451 phenethylamine, butylamine, hexylmethylamine, and cesium iodide (CsI, 99.9%) were all
452 purchased from Sigma Aldrich. Formamidinium iodide (FAI) and methylammonium chloride
453 (MACl) were purchased from Xian-Polymer. Lead iodide (PbI₂, ultra-dry) was purchased from

454 Alfa Aesar. 4-Hydroxybenzylammonium salts were purchased from Alfa-chemical. 2PACz ([2-
455 (9H-carbazol-9-yl)ethyl]phosphonic acid, >98.0%) and MeO-2PACz were purchased from TCI.
456 4PADCB (4-(7H-dibenzo[c,g]carbazol-7-yl)butyl)phosphonic acid) was purchased from
457 Dyenamo. C₆₀ (>99.5% purity) and bathocuproine (BCP, >99%) were purchased from Ossila Ltd.

458 **Device fabrication**

459 Glass/ITO substrates were washed in first acetone and then isopropyl alcohol for 20 min of each.
460 After washing, the substrates were dried and treated with UVO prior to use for 10-20 min. The
461 hole-transporting SAM (1 – 2 M) or mixed SAMs+2D-ligands (1:0.5, 1:1, 1:1.5, and 1:2 molar
462 ratio) were dissolved in ethanol. Then, the solution was spin-coated onto glass/ITO at 5000 rpm
463 for 30 s in a nitrogen-filled glovebox. After thermal annealing at 100 °C for 10 min, the hole-
464 selective layer coated ITO was cooled down and washed by ethanol by dynamic coating at 5000
465 rpm for 30 s to remove unbounded molecules.

466 A perovskite precursor solution (~1.5 M) of Cs_{0.025}MA_{0.075}FA_{0.90}PbI₃ was prepared by mixing FAI,
467 MAI, CsI, and PbI₂ with a molar ratio of 0.90:0.075:0.025:1 and then dissolving them in a mixed
468 solvent of DMF and DMSO (4:1 vol. ratio). 15 mol% of MACl was also added. For
469 Cs_{0.05}FA_{0.95}PbI₃ was prepared by mixing FAI, CsI, and PbI₂ with a molar ratio of 0.95:0.05:1 and
470 then dissolving them in a mixed solvent of DMF and DMSO (4:1 vol. ratio) to get ~1.5 M. Then,
471 around 10 mol% of MACl and 2 mol% of KCl were also added in the mixed perovskite solution.
472 The mixture of precursor solutions was shaken by a vortex shaker overnight at room temperature
473 until fully dissolved.

474 The perovskite precursor solution was spin-coated at 2000 rpm for 40 s and 6000 rpm for 10 s. At
475 the 10th s, 200 mL of anisole was dropped onto the films by the end of the spin-coating process.
476 Then, the films were annealed at 120 °C for 30 min to form the perovskite layer. For 2D perovskite
477 passivation at the top side, at the first step, PbI₂ beads were thermally evaporated (10⁻⁶ Torr) at an
478 evaporation rate of 0.5 Å s⁻¹ to get thickness around 7, 15, and 25 nm. The second step is dropping
479 HBzA salt solution or mixture HBzA salt: FAI solution with 1:1 molar ratio (in mixture IPA and
480 DMF, 98:2 vol%) and then spin-coated at 2000 rpm for 30 s, followed by thermal annealing at
481 100 °C for 10 min. After this process, the perovskite films were stored overnight in vacuum
482 condition. All the process is done under N₂-glovebox with O₂ level was <10 ppm and H₂O level
483 was <0.1 ppm. Then the samples were transferred into a thermal evaporator for the C₆₀ (25 nm)

484 and BCP (3 nm) deposition. For the final step, a 120 nm thick Ag layer was evaporated at low
485 pressure ($<10^{-6}$ Torr) with an area of ~ 0.1 cm². A ~ 120 nm MgF₂ was also evaporated at the glass
486 side to minimize the reflection losses from the glass substrates.

487 **Device Analysis**

488 The J - V curves were recorded using a Keithley 2400 source unit under AM 1.5 G (100 mW cm⁻²)
489 illumination with an Abet Technologies Sun 3000 solar simulator. The spectral mismatch was
490 calibrated using a KG-5 filter-covered mono-silicon standard cell (Newport). All devices were
491 measured in nitrogen filled glovebox for a sweep mode of reverse and forward scans with a
492 scanning rate of 0.1 V s⁻¹. The stabilized output of the devices was acquired by recording the power
493 output of the illuminated device at a constant voltage near the MPP extracted from the J - V curve.
494 External quantum efficiency spectra were obtained by passing the output of a 400 W Xenon lamp
495 through a monochromator and filter. Calibration was performed with a 603621 Calibrated Silicon
496 and Germanium Reference Detector. Activation energy measurement of ion migration. Electrical
497 poling was performed by applying different biases to the devices for 1 min in the dark; current-
498 voltage were measured with a Keithley 2401 source. Temperature dependence was measured with
499 a CTI cryogenic probe station with an attached Lakeshore 331 temperature controller under
500 vacuum (1×10^{-4} Pa). The temperature was monitored using a thermocouple placed in contact with
501 the sample. During the measurement, devices were first cooled to 10 K for 10 min and then heated
502 to adjust the temperature. The temperature was stabilized for 5 min prior to recording the current
503 for each step. Cross-section KPFM measurements were carried out using a home-built system
504 based on Bruker Dimension Icon atomic force microscope. The sample preparation and
505 measurements were conducted inside an Ar-filled glovebox. We used a Pt-Ir coated silicon probe
506 (PPP-EFM) and operate in tapping mode. The mapping was performed with 1024 pixels in the
507 fast-scan axis and more than 32 lines in the slow-scan axis, at a scan rate of 0.35 Hz. To ensure a
508 flat surface and expose all layers of the device, the cell was directly cleaved without polishing or
509 ion-milling. We then mapped the surface potential at the same location under dark and LED
510 illumination, with the LED providing white light of approximately 1 Sun intensity. To reduce the
511 noise level, we averaged the electrical potential profiles from all slow-scan lines. Next, we
512 subtracted the dark potential from the illuminated condition and calculated the first derivative to
513 obtain the electric field distribution across the device.

514 **Sample Characterization**

515 Field-emission SEM images were obtained with a JSM-7610F device (JEOL Ltd.). The PL
516 emission was spectrally resolved using collection optic. For STEM based study, cross-sectional
517 electron-transparent lamella was prepared in focused ion beam (FIB) equipped SEM-FIB Helios
518 G4 DualBeam, FEI with help of an EasyLift nanomanipulator and Ga ion source. First protect the
519 region of interest during FIB, two types of protective coatings were deposited: a 0.5 μm layer of
520 Pt coating deposited by the e-beam, followed by a 3 μm layer of Pt coating deposited by the ion
521 beam for final protection. Step by step ion beam milling procedure with beam current (2.4, 0.44,
522 0.26, 0.045, 0.025 nA for 30 to 5 kV) was carried out by cutting and thinning down lamella to 60
523 nm, while decreasing beam current (till 0.025 nA at 2 kV) to avoid ion beam damage. Additionally,
524 low current cleaning process (5-2 kV, 81-28 pA) was performed to remove any potential
525 contamination. STEM based experiments such as HAADF-STEM were performed in Cs Prob-
526 corrected ThermoFisher Titan 60-300 Cubed TEM microscope operating at 300 kV. TEM data
527 processing was performed using Gatan™ Digital Micrograph and Thermo Scientific™ Velox
528 suites. For TEM and PL characterizations, the perovskite film samples preparation used 1:2 molar
529 ratio of SAM and 2D ligand to help observation of 2D perovskites.

530 GIWAXS was conducted in the PLS-II 6D UNIST-PAL beamline of the Pohang Accelerator
531 Laboratory (PAL), Korea. The energy of X-rays from the bending magnet was monochromatized
532 to 18.986 keV (0.6530 \AA) using a double-crystal monochromator. The 2D charge-coupled device
533 detector (MX225-HS, Rayonix, LLC, USA) was used to record the 2D GIWAXS pattern, and the
534 GIWAXS sample chamber was equipped with a 5-axis motorized stage for fine sample alignment.
535 The sample-to-detector distance was 242.58 mm, and the diffraction angles were calibrated using
536 NIST SRM660b, lanthanum hexaboride (LaB₆). Incidence angle of $\sim 0.2^\circ$ was used for the
537 GIWAXS measurements to obtain crystallographic information on the perovskite films used in
538 this work.

539 XPS/UPS measurements were performed in a UHV chamber (ScientaOmicron) operating at a
540 pressure of 5×10^{-10} mbar. UPS measurements were carried out using a 21.2 eV vacuum UV
541 source (focus). The sample was biased by 10 eV to observe the low kinetic energy cutoff. The
542 photoelectrons were collected at an angle of 80° between the sample and analyzer, with a normal
543 electron take off angle. The constant analyzer pass energy was 5 eV for the valence band region

544 and for the secondary electron cut-off. XPS was carried out in the same spectrometer, equipped
545 with a monochromatic Al Ka X-ray Omicron XM1000 X-ray source ($h\nu = 1486.6$ eV) operating
546 at a power of 390 W. The high-resolution spectra were collected at a CAE of 15 eV. The spectra
547 were analyzed with Casa XPS software. The individual peak envelopes were fitted by a Gaussian
548 –Lorentzian (GL30) using a Tougaard based background function. Fourier-transform infrared
549 spectroscopy (FTIR) was conducted using Cary 600 Series FTIR Spectrometer (Agilent Tech.)
550 equipped with PIKE GladiATR geometry using diamond crystal in transmission mode. Samples
551 of powder were first dissolved into ethanol solvent and dried in a vacuum, then annealed at 100 °C
552 under N₂-glovebox for 10 min to completely remove the solvent. The dried powder samples are
553 spread uniformly above the crystal surface of FTIR. The spectral resolution was set to 4 cm⁻¹ and
554 obtained by averaging 20 scans of each measurement. Transient PL decay and PLQY were
555 recorded using a spectrofluorometer (Fluoroma-Modular, Horiba Scientific). The 520 nm
556 calibrated pulse laser was generated from a picosecond laser diode (PicoQuant) equipped band-
557 pass 650 nm filter to collect 795 nm emitted light. The fluence is estimated to be around ~10
558 nJ/cm². For PLQY, an integrating sphere (Fluorolog, Horiba JobinYvon) was used and compared
559 with different tools using a JASCO FP-8500 spectrofluorometer equipped with an ILF-835
560 integrating sphere with the same procedure. It is noted that the results were consistent from two
561 different setups and measurements, confirming our reliability results as given in the statistical
562 PLQY values with a small deviation standard in Extended Data Fig. 6a.

563 **Device stability testing**

564 For the stability test, ~10 nm layer of tin (IV) oxide and an 80 nm layer of indium zinc oxide were
565 deposited on top of the C₆₀ sequentially, by atomic layer and sputtering depositions, respectively,
566 to replace the BCP layer. The operational stability tests were carried out at the MPPT for the
567 encapsulated devices under 1 sun in ambient air (RH >50 %) at ~40 °C. The voltage at the MPPT
568 was automatically applied, and the power output of the devices was tracked. For the open-circuit
569 light soaking test, the devices were kept under full 1 sun illumination and constant temperature at
570 85 °C on hotplate in ambient air (RH above 50 %). The devices then measured periodically until
571 1000 h. The devices were encapsulated with simple glass and epoxy method. All processes were
572 done in N₂ glovebox.

573

574 **Acknowledgement.**

575 This work was supported by the King Abdullah University of Science and Technology (KAUST)
576 Office of Sponsored Research (OSR) under award nos. OSR-2021-4833, OSR-CARF/CCF-3079,
577 IED OSR-2020-4611, IED OSR-2019-4580, OSR-CRG2020-4350, OSR-2020-CPF-4519,
578 OSR438 CRG2019-4093, IED OSR-2019-4208, HERO. We acknowledge the use of KAUST
579 Solar Center and Core Lab facilities and the support from its staff. We thank KPV Lab members,
580 Helen Bristow, Maxime Babics, Shruti Sarwade, Asmat Ullah, etc. for their support. A.M.R. and
581 S.I.S. acknowledge financial support from the Basic Science Research Leaders Program of the
582 National Research Foundation of Korea (NRF) (Grant NRF-2018R1A3B1052820).

583 **Author contributions**

584 R.A. conceived, directed the research, and wrote the original draft. R.A., D.S.U., I.F.I, and A.P.
585 fabricated the solar cells. B.V. conducted FIB and TEM measurements and analyses. A.M.R.
586 performed the GIWAXS measurement and analysis. R.A. and A.M.R. performed PLQY
587 measurement and analysis. S.Z. contributed to conceptualizing the idea of 2D perovskite and
588 discussion at the bottom contact. P.D. performed XPS, IPES, and UPS measurements and did data
589 analysis. R.A., D.S.U., and E.U. performed optical spectroscopy measurements and data analysis.
590 D.S.U. performed SEM measurements. A.P. performed the top-surface KPFM measurement and
591 did data analysis. R.A. performed and analysed the electronic characterization of the devices. F.C.
592 performed cross-section KPFM and analysis. D.U. and A.A.S. performed the FTIR and analysis.
593 I.F.I. helped to synthesized and characterized 2D perovskite layers. I.F.I. and A.A.S. performed
594 the XRD measurement analysis. A.R.P. fabricated the aperture mask and determined the area.
595 A.A.S. and A.S.S. helped to review the manuscript. E.A. contributed to reviewing and writing the
596 manuscript. S.I.S. and C.X. supervised the project. S.D.W. supervised the overall project and
597 secure the funding. All authors contributed to the manuscript.

598 **Conflicts of Interest**

599 The authors declare no competing interests.

600 **Data availability**

601 The data sets generated during and/or analysed during the current study are available from the
602 corresponding author upon request.

603 Extended Data Figure legends

604 **Extended Data Fig. 1: Chemical analysis of SAMs and HBzA ligand.** **a**, Photograph of the
605 mixture 2PACz:HBzA (1:1 molar ratio) compound after drying under vacuum for a few days and
606 then annealed at 100 °C in a nitrogen glovebox to completely remove the solvent. The yellow
607 precipitated powder indicates the protonation between the first P–OH of the phosphonic group of
608 2PACz and the amine of HBzA molecules, forming an ionic bond. **b**, FTIR peaks of HBzA,
609 2PACz, and mixture (2PACz:HBzA, 1:1 molar ratio) in solid-state powder. The shifting peaks of
610 P–OH at $\sim 950\text{ cm}^{-1}$ and $\sim 1033\text{ cm}^{-1}$ to the higher wavenumber of the mixture compound indicate
611 stronger bonding due to deprotonation of the first P–OH group of the phosphonic acid of 2PACz.
612 Consequently, the additional new peak associated with the P–O bond at 1105 cm^{-1} is formed. In
613 contrast, N–H bending peaks of the amine group (HBzA) at $\sim 1530\text{ cm}^{-1}$ and 1620 cm^{-1} are shifted
614 to the lower wavenumber with enhanced intensity in the mixture compound, presumably due to
615 the protonation of $-\text{NH}_2$ to $-\text{NH}_3^+$. These results successfully confirm the acid-base reaction
616 between the pK_{a1} of the phosphonic acid and the pK_b of alkyl amines, as illustrated in **Fig. 1a**. **c**,
617 XPS analysis of 2PACz on ITO film. High-resolution spectra of C1s of 2PACz, HBzA, and a
618 mixture of 2PACz+HBzA onto ITO after washing with DMF/DMSO.

619 **Extended Data Fig. 2: SKPM mapping images and distributions of WF.** **a**, ITO/2PACz+HBzA
620 sample before and after washing. The DMF/DMSO solvent mixture was used to wash the
621 ITO/2PACz+HBzA sample. The minor WF shifting of the ITO/2PACz+HBzA sample before and
622 after washing with DMF/DMSO indicates a strong attachment of HBzA molecules onto 2PACz
623 molecules, consistent with XPS results. **b**, ITO/2PACz sample after washing. **c**, Bare ITO. **d**,
624 SKPM mapping images of ITO/2PACz/perovskite and ITO/2PACz+HBzA/perovskite samples
625 after washing with DMF/DMSO. **e**, Distributions of WF of both samples from KPFM
626 measurement. After the perovskite film deposition and subsequent removal of the HBzA ligands,
627 the WF of ITO/2PACz+HBzA is shifted back to the WF of pristine ITO/2PACz ($\sim 5.40\text{ eV}$),
628 confirming our hypothesis.

629 **Extended Data Fig. 3: Statistics of PCE, V_{oc} , and FF of PSCs.** **a**, Bottom-side 2D/3D with
630 different molar ratios of 2PACz: HBzA. **b**, Bottom-side 2D/3D with various 2D ligands
631 (benzylamine, BzA; phenethylamine, PEA; butylamine, BA; hexylmethylamine, HMA) for
632 bottom-side 2D/3D heterojunction with a 1:1 molar ratio of 2PACz. **c**, Top-side 3D/2D with PbI_2
633 thickness variation for top-side 3D/2D heterojunction. The statistics are obtained from 10 to 20
634 cells for each condition from different batches. It is noted that the perovskite used here is based on
635 $\text{Cs}_{0.05}\text{FA}_{0.95}\text{PbI}_3$.

636 **Extended Data Fig. 4: Energetic alignment analysis.** **a**, Energy level scheme for 2PACz
637 anchored on ITO, 3D-perovskites, 2D-perovskites on top and bottom interfaces, and C_{60} layers
638 extracted from UPS data. The VBM was obtained as $h\nu - (E_{\text{cutoff}} - E_{\text{VB, min}})$. The position of the
639 CBM with respect to the VBM was defined by extracting E_g ($\sim 1.53\text{ eV}$) from EQE in
640 Supplementary Fig. 8 for 3D-perovskite and by IPES for 2D-perovskite with $n = 2$ ($E_g = \sim 2.1\text{ eV}$).
641 **b**, **c**, Secondary electron cut-off and valence spectra plots from UPS measurement. **d**, IPES spectra
642 of the 2D perovskite film with $n = 2$ using the hybrid method.

643 **Extended Data Fig. 5: Device performance with double-cation perovskite.** **a**, Representative
644 J - V curve for control and double-side 2D/3D heterojunctions perovskite solar cells with

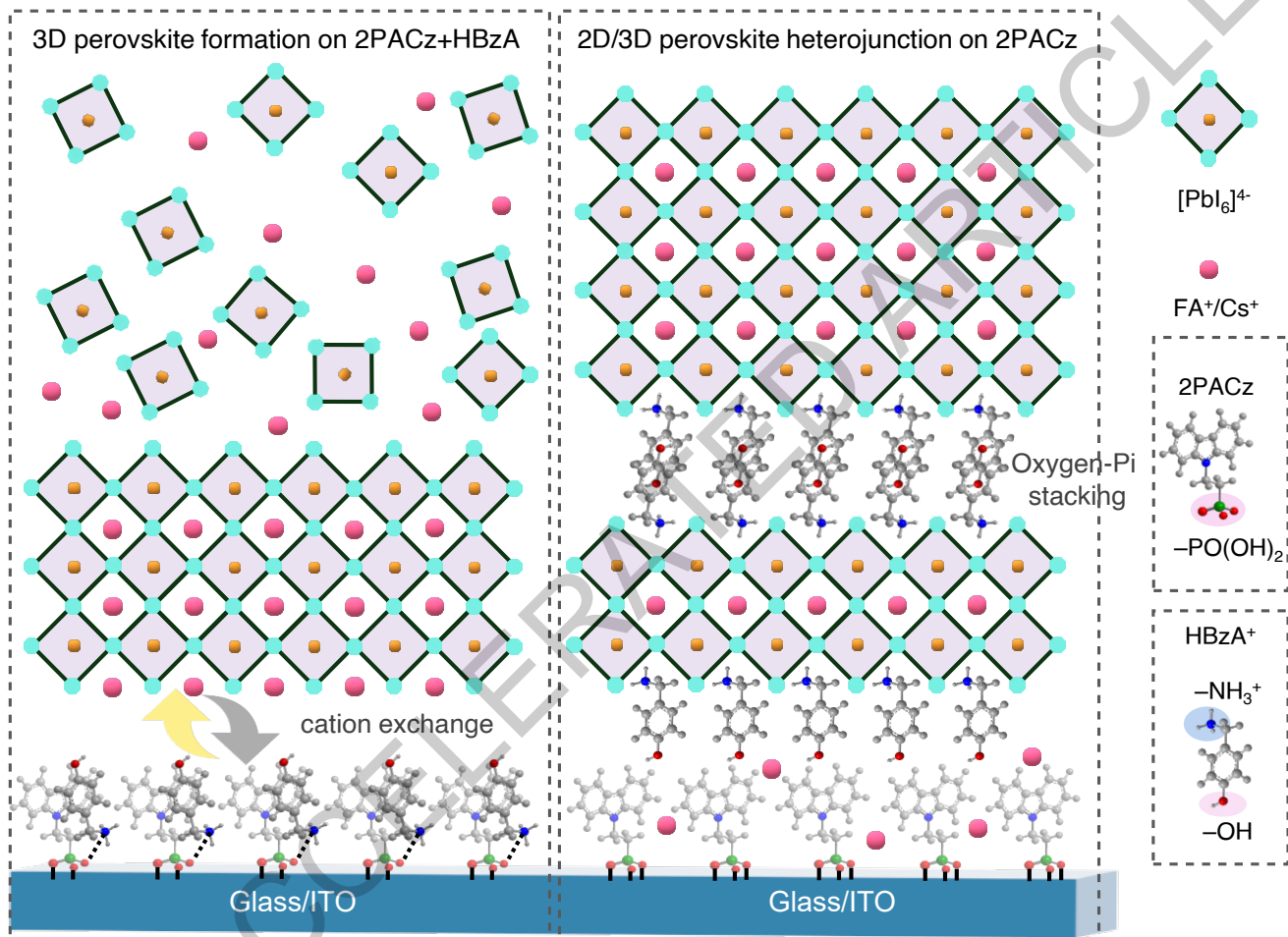
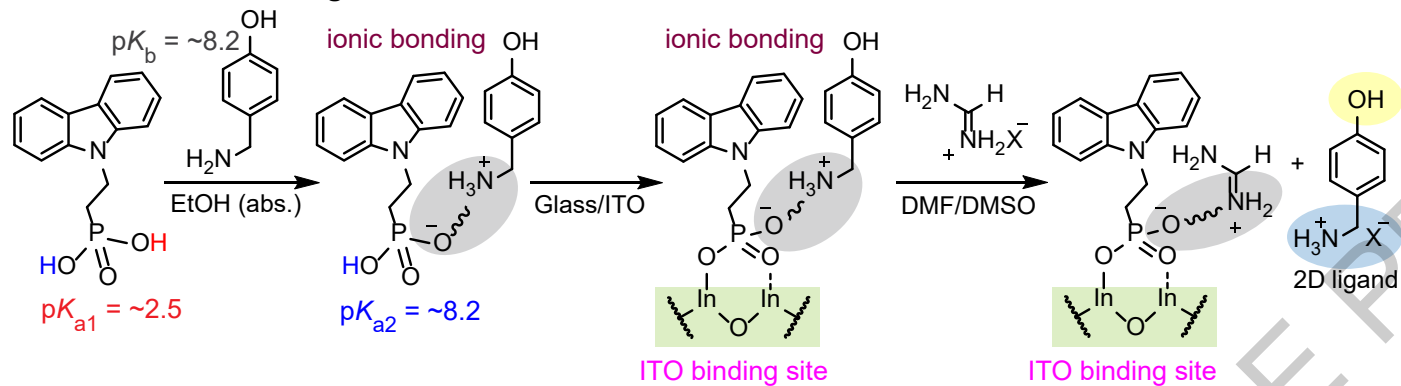
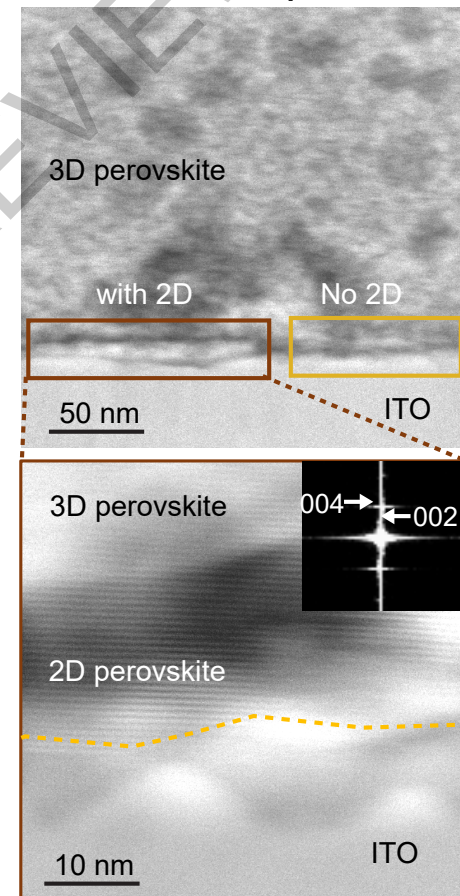
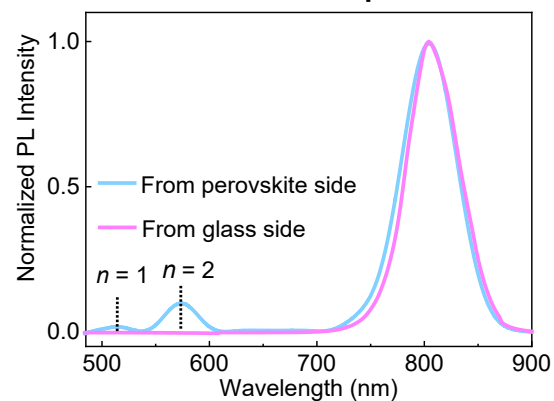
645 $\text{Cs}_{0.05}\text{FA}_{0.95}\text{PbI}_3$ perovskite, achieving a maximum PCE of 25.2% under reverse scan. Statistical
646 parameters of (b) PCE, (c) V_{OC} , and (d) FF values of PSCs. The statistical parameters are obtained
647 from 50 cells for each condition from different batches.

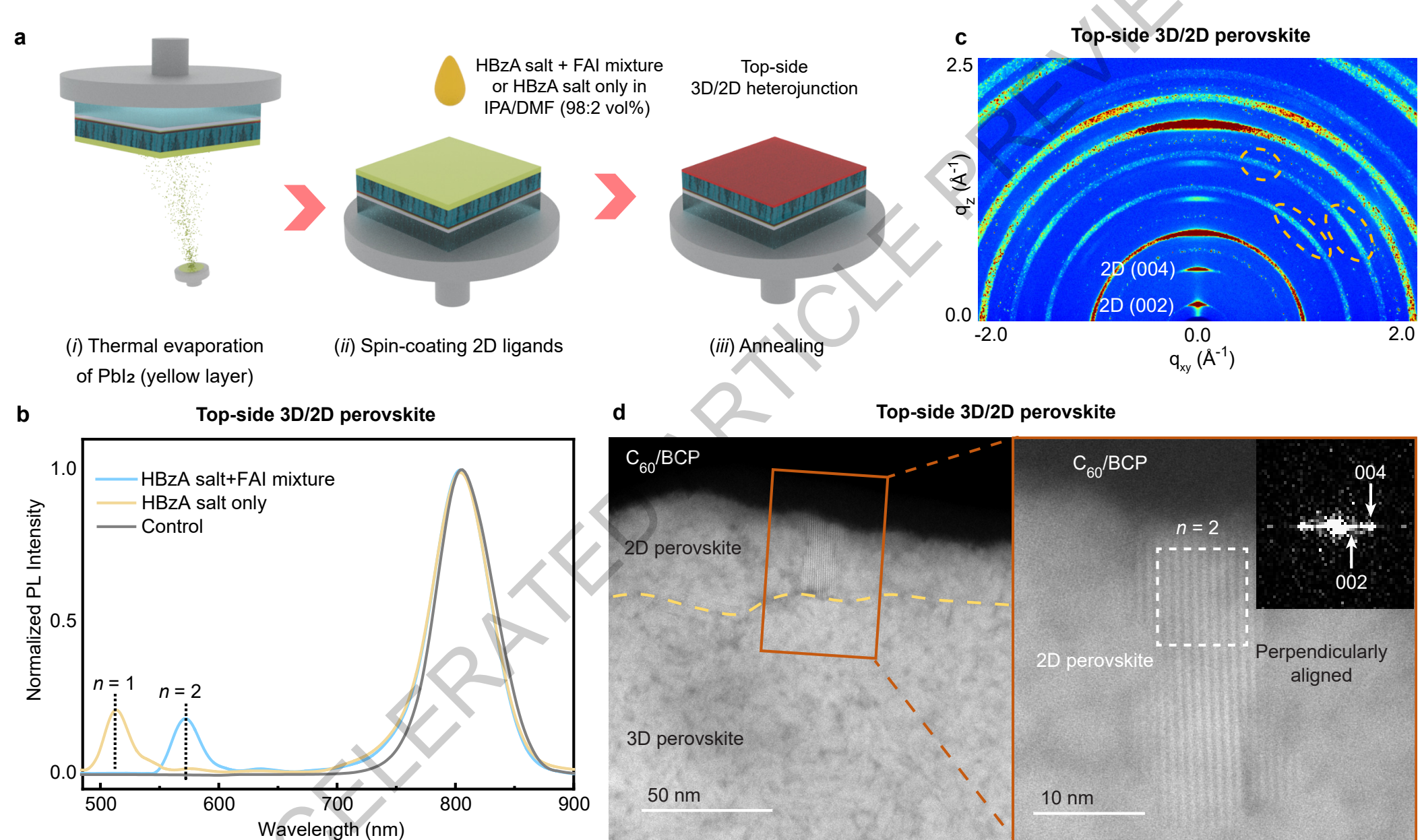
648 **Extended Data Fig. 6: Passivation and trap analysis.** a, PLQY results, and (b) transient PL
649 decays of perovskite films on various 2D/3D heterojunctions. c, d, SCLC plots for control and
650 double-side 2D/3D heterojunction-based devices of (c) electron-only and (d) hole-only devices. e,
651 TAS analysis of control, bottom-side, and double-side 2D/3D passivation-based devices.

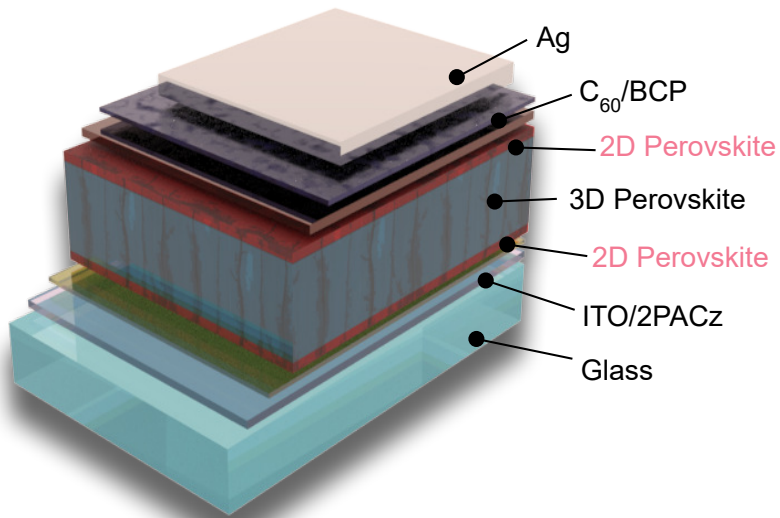
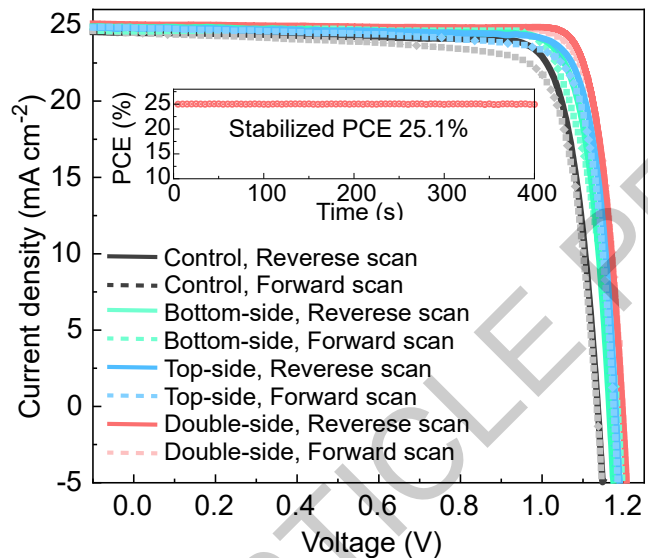
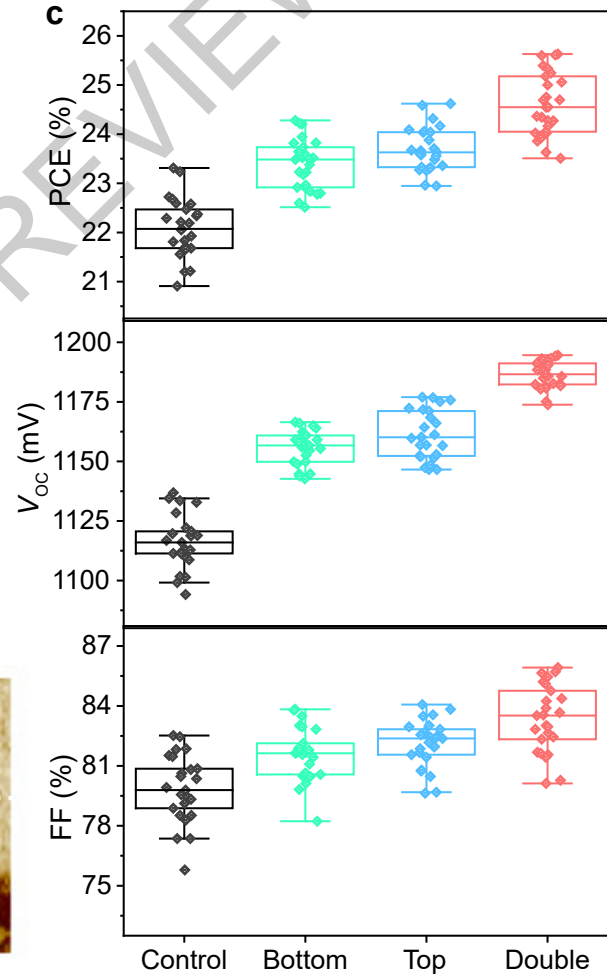
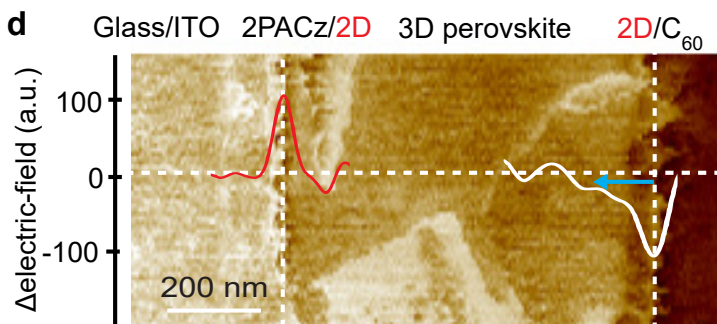
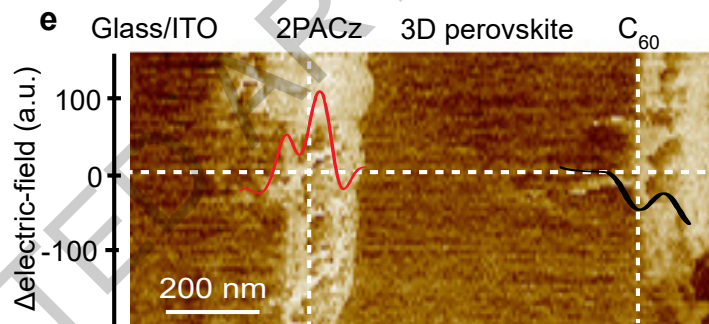
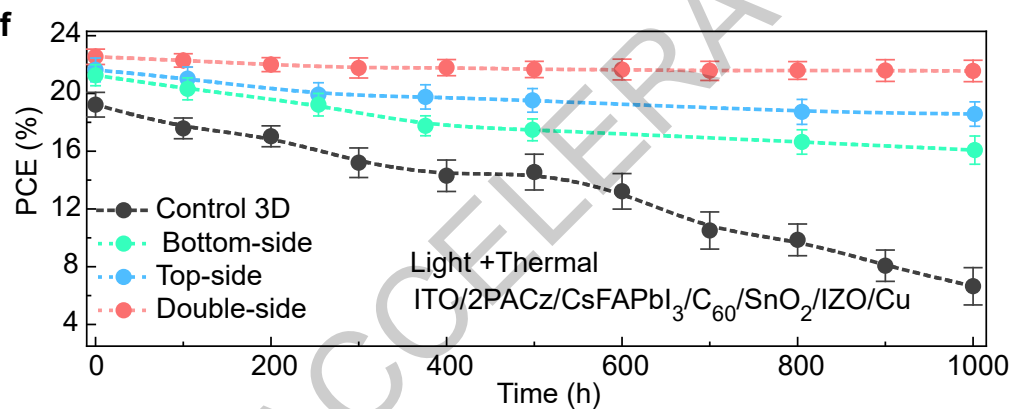
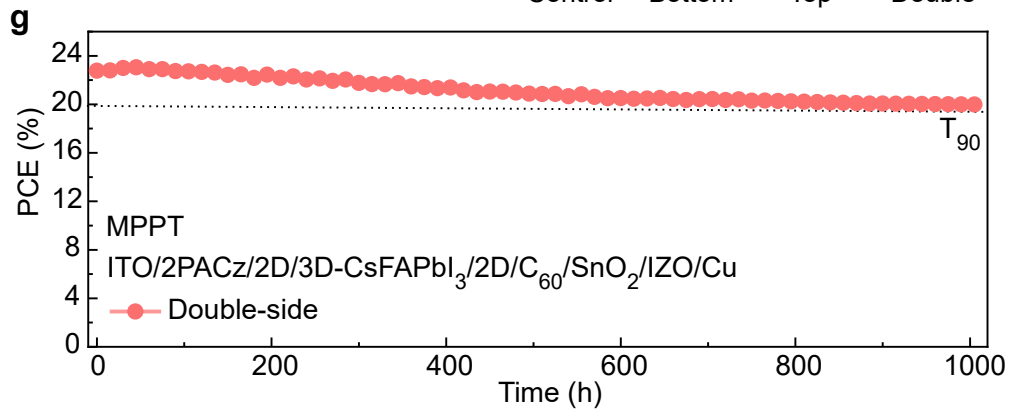
652 **Extended Data Fig. 7: Stability and ion migration analysis.** a, b, UV-vis absorbance spectra
653 evolution of iodine in toluene solution for the control (a) and double-side passivation of perovskite
654 films (b) at different aging times. Inset is a photo of the sealed vials with the control and 2D/3D
655 perovskite films, taken after 100 h of light and heat exposures. c, Temperature-dependent
656 conductivity of control and double-side 2D/3D perovskite films.

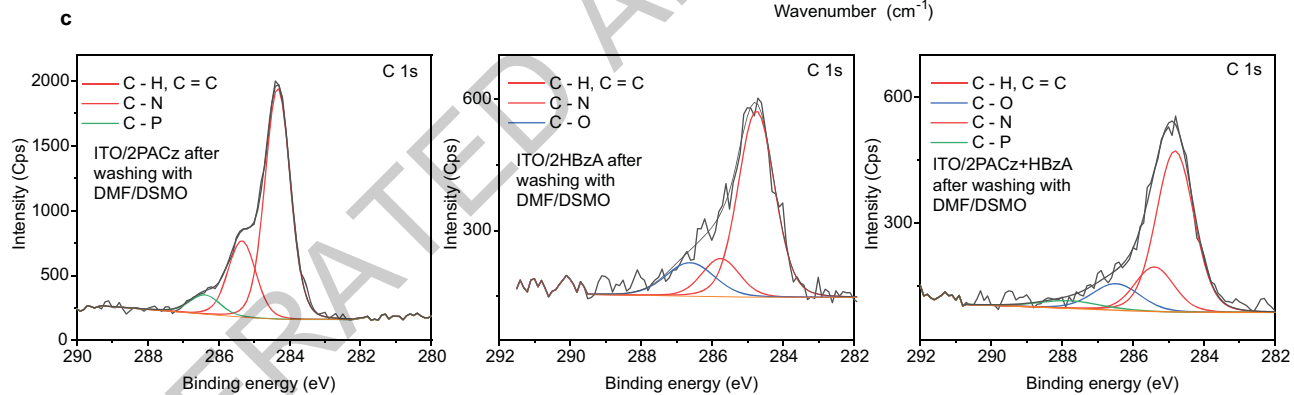
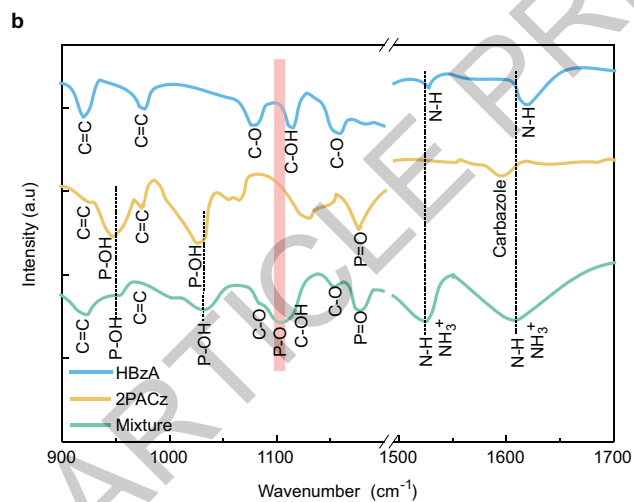
657

ACCELERATED ARTICLE PREVIEW

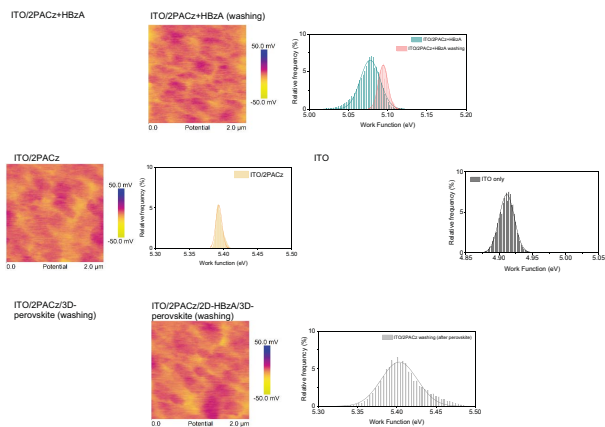
a Mechanism of 2D ligand formation and release from the ITO/2PACz surface**b Bottom-side 2D/3D perovskite****c Bottom-side 2D/3D perovskite**



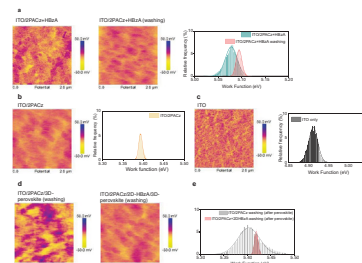
a**b****c****d****e****f****g**



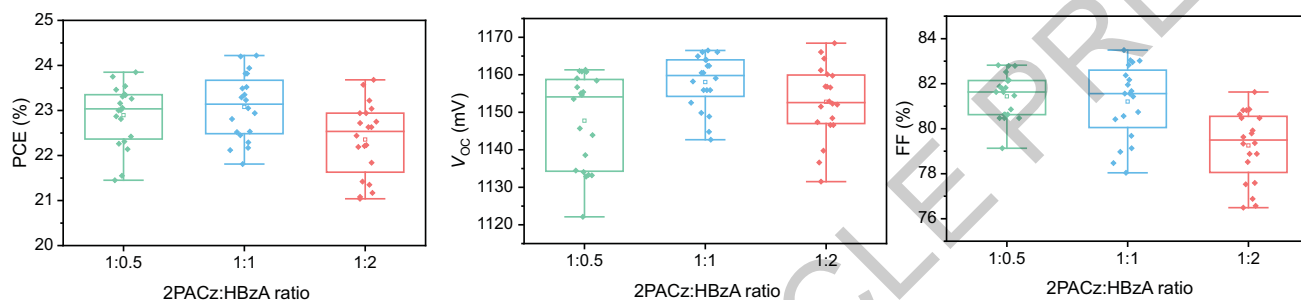
Extended Data Fig. 1



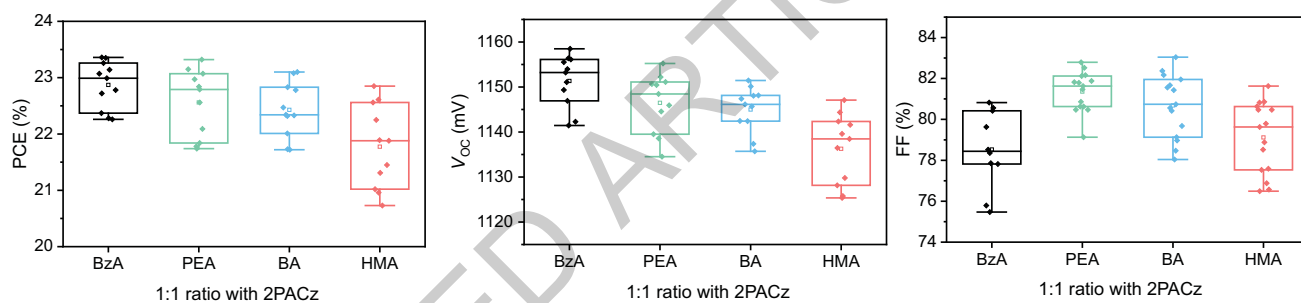
Extended Data Fig. 2



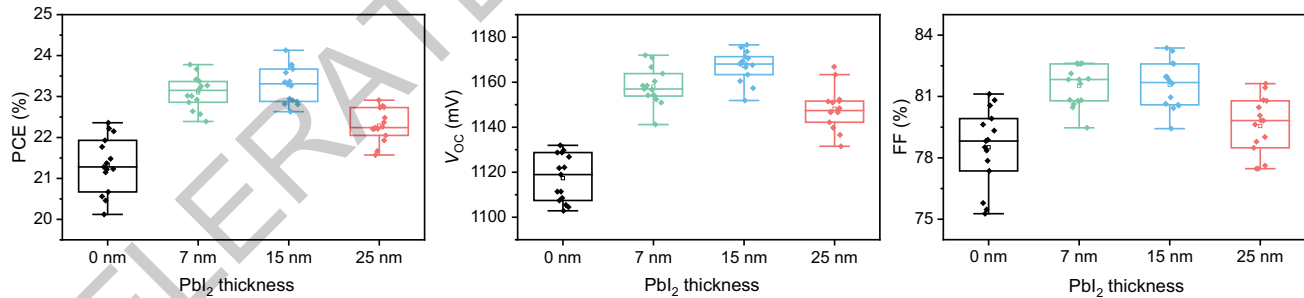
a Bottom-side 2D/3D heterojunction



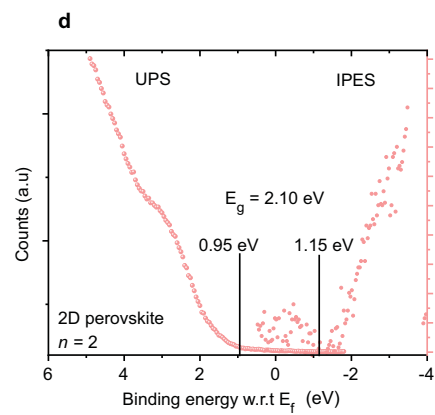
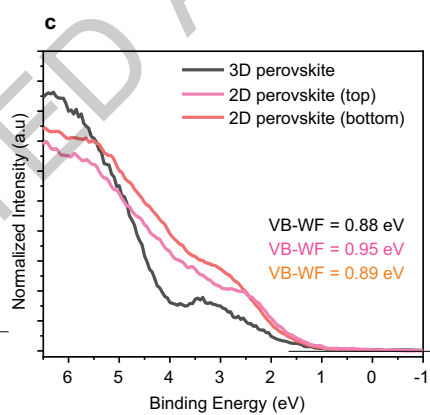
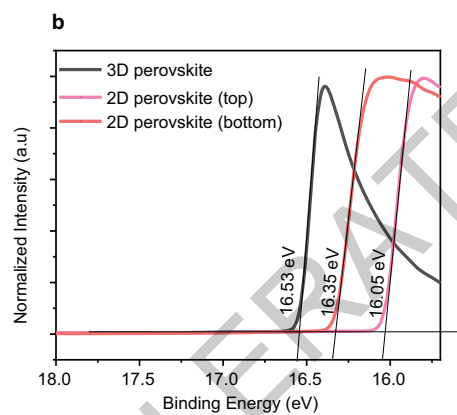
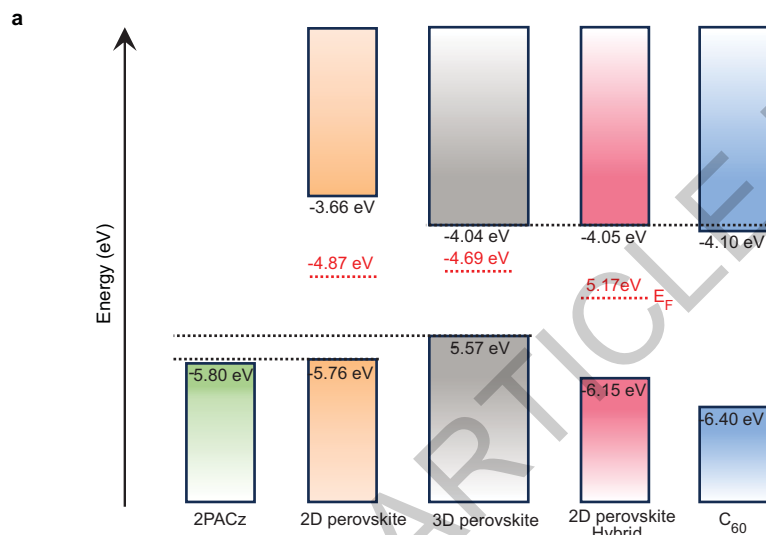
b 2D/3D at bottom with various ligands



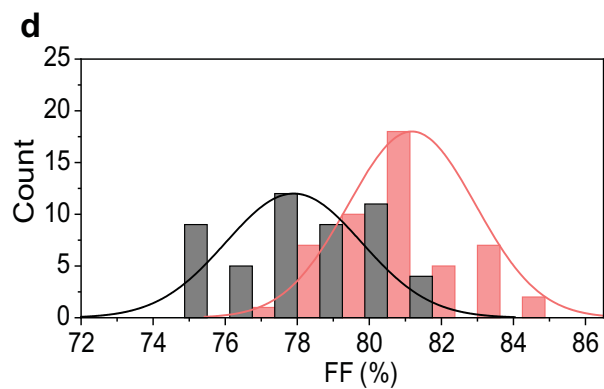
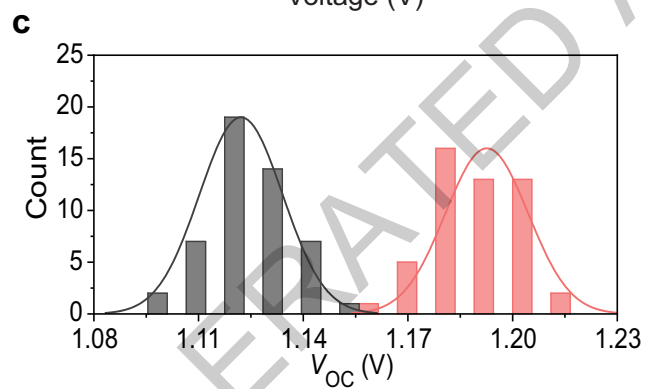
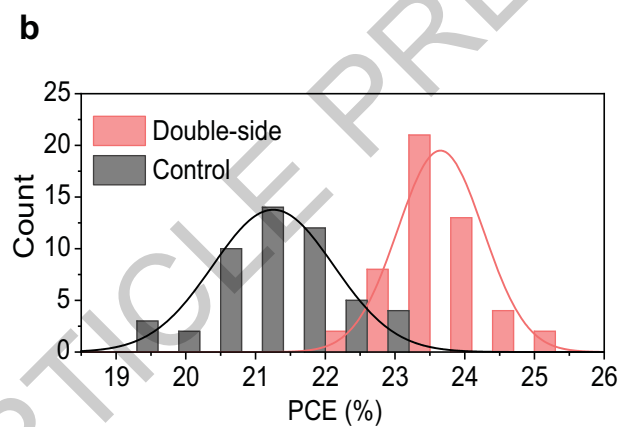
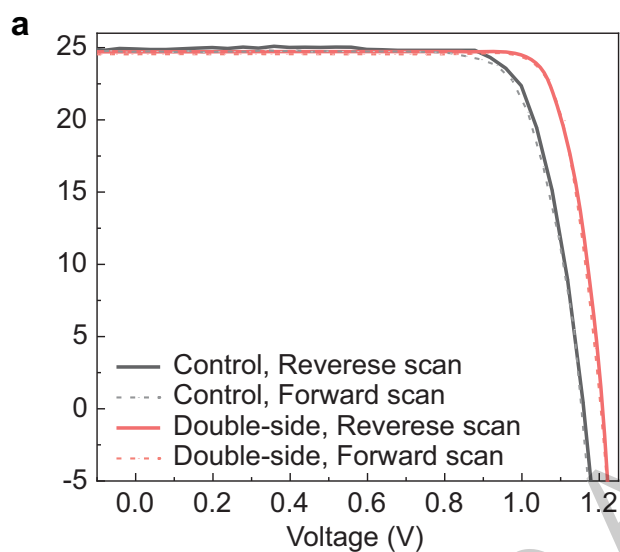
c Top-side 3D/2D heterojunction



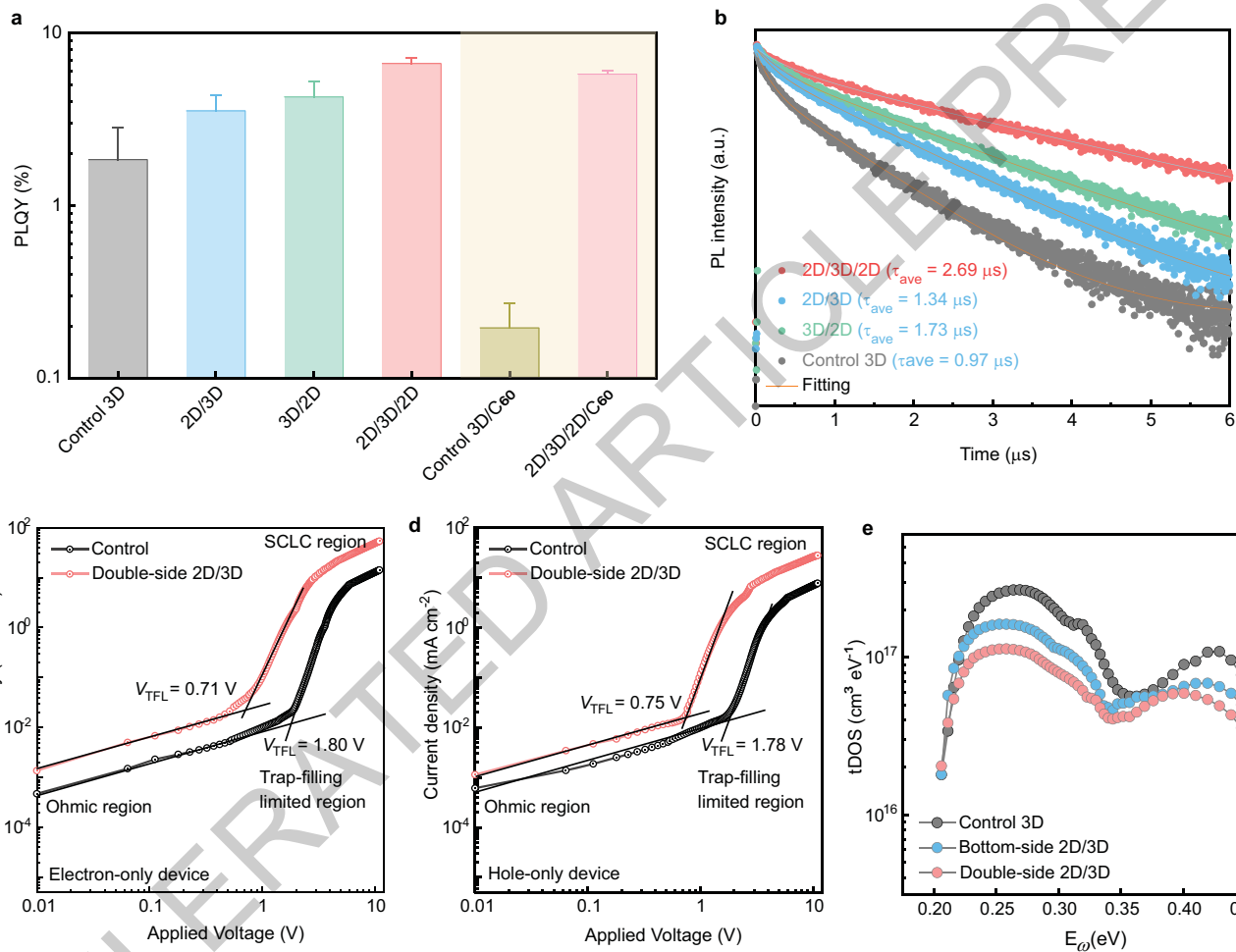
Extended Data Fig. 3



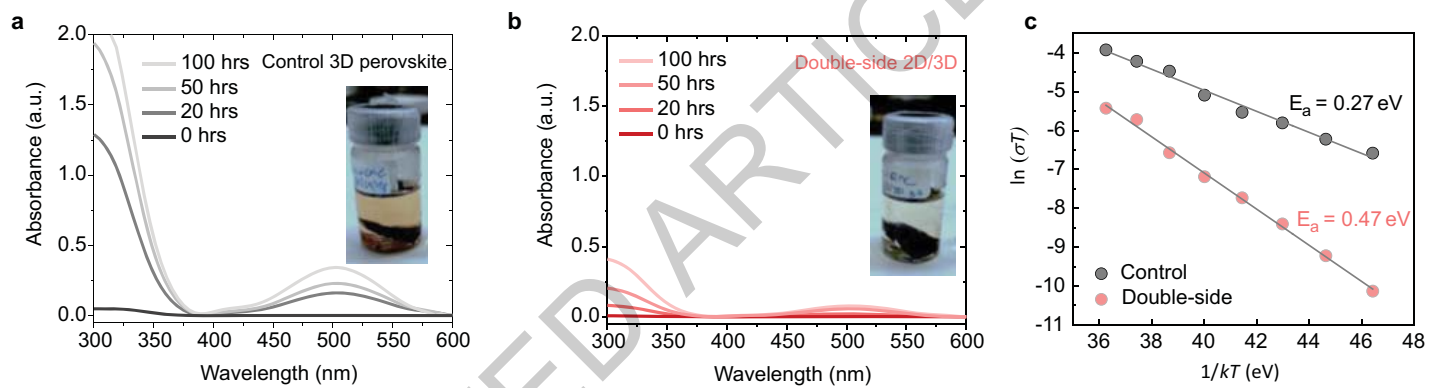
Extended Data Fig. 4



Extended Data Fig. 5



Extended Data Fig. 6



Extended Data Fig. 7